ADVANCED OPTICAL MATERIALS
www.advopticalmat.de

Nanoscale Mapping and Defect-Assisted Manipulation of Surface Plasmon Resonances in 2D Bi_2Te_3/Sb_2Te_3 In-Plane Heterostructures

*Parivash Moradifar, Austin G. Nixon, Tiva Sharifi, Tim Brandt van Driel, Pulickel Ajayan, David J. Masiello, and Nasim Alem**

The Bi_2Te_3/Sb_2Te_3 in-plane heterostructure is reported as a low-dimensional tunable chalcogenide well suited as plasmonic building block for the visible–UV spectral range. Electron-driven plasmon excitations of low-dimensional Bi_2Te_3/Sb_2Te_3 are investigated by monochromated electron energy loss spectroscopy spectrum imaging. To resolve the nanoscale spatial distribution of various local plasmonic resonances, singular value decomposition is used to disentangle the spectral data and identify the individual spectral contributions of various corner, edge, and face modes. Furthermore, defect-plasmon interactions are investigated both for nanoscale intrinsic and thermally induced extrinsic polygonal defects (in situ sublimation). Signature of defect-induced red shift ranging from a several hundreds of millielectronvolts to a few electronvolts, broadening of various plasmon response, together with selective enhancement and significant variations in their intensity are detected. This study highlights the presence of a heterointerface and identifies defects as physical tuning pathways to modulate the plasmonic response over a broad spectral range. Finally, the experimental observations are compared qualitatively and validated with numerical simulations using the electron-driven discrete dipole approximation. Low-dimensional Bi_2Te_3/Sb_2Te_3 as a less explored plasmonic system holds great promises as emerging platform for integrated plasmonics. Furthermore, introducing controlled structural defects can open the door for nanoengineering of plasmonic properties in such systems.

1. Introduction

Surface plasmons are the collective excitations of conduction-band electrons formed at the interface of two materials with significant optical contrast, such as at a metal/dielectric interface. Upon excitation, surface plasmons enable enhancement, confinement, and manipulation of incident light at the nanoscale level.[1–6] The unique optical properties of surface plasmons have offered transformative solutions for a wide range of high impact applications in ultra-efficient nanostructured solar cells, ultra-fast data transport, and photothermal biomedical therapeutic applications.[5–7]

Supporting strong field enhancement in the visible spectral range (1.7–3.2 eV), noble metal-based (Ag, Au) nanostructures are the most widely studied plasmonic materials.[8] However, strong dissipation originating from interband electronic transitions and Drude losses in noble metal-based nanostructures, makes it imperative to investigate alternative plasmonic building blocks.[9] This has inspired an intense search for new low-loss materials that can support plasmonic excitations particularly in the visible range and into the UV regime.[1,10–12]

Recently, 2D materials and group V–VI chalcogenides known for their excellent thermoelectric and topological insulator (TI) properties, have attracted considerable attention due to their active plasmonic properties with potentially lower losses.[10] In these systems, bulk carriers

P. Moradifar, N. Alem
Department of Materials Science and Engineering
Materials Research Institute
The Pennsylvania State University
University Park
PA 16802, USA
E-mail: nua10@psu.edu

A. G. Nixon, D. J. Masiello
Department of Chemistry
University of Washington
Seattle, WA 98195, USA

T. Sharifi, P. Ajayan
Department of Materials Science and Nano Engineering
Rice University
Houston, TX 77005, USA

T. Sharifi
Department of Physics
Umeå University
Umeå 90187, Sweden

T. B. van Driel
SLAC National Accelerator Laboratory
Menlo Park, CA 94025, USA

The ORCID identification number(s) for the author(s) of this article can be found under https://doi.org/10.1002/adom.202101968.

DOI: 10.1002/adom.202101968

(nonequilibrium carriers from interband transitions) and surface charge carriers (gapless metallic surface states in topologically protected surface states) are the two major contributors for potential metal-like plasmonic behavior.[13,14] Therefore, among the 2D crystal family, TI chalcogenide systems can be considered as promising candidates for plasmonic alternatives beyond gold and silver with thermoelectric and topologically insulating properties serving multiple thermal and optoelectronic applications.[1,8,9,15]

In the last decade, a few TI-based nanostructures such as Sb_2Te_3 thin films,[16] Bi_2Se_3 nanoflowers and nanoplatelets,[17–19] chemically intercalated Bi_2Se_3 nanoplatelets,[20] $Bi_{1.5}Sb_{0.5}Te_{1.8}Se_{1.2}$ metamaterials,[1,10] and Bi_2Te_3 nanoplatelets[7,21] have been experimentally investigated. These studies exhibit plasmonic responses in a broad-spectral region from the visible to UV regime. In particular, for 2D Bi_2Te_3 nanoplates multiple distinct plasmon modes have been observed in the visible range.[21] Bi_2Te_3 is a narrow band gap semiconductor (band gap: ≈0.15 eV) with a rhombohedral crystal structure and space group of $R\overline{3}m$. Bi_2Te_3 has a layered structure consisting of five alternating atomic layers of Bi and Te (Te(1)-Bi-Te(2)-Bi-Te(1)) arranging in ABC order along the *c*-axis. The alternating layers are bonded covalently, forming charge-neutral quintuple layers (QLs) with 1 nm thickness. However, neighboring QLs are predominantly bound by weak van der Waals interactions, making it easy to cleave the crystal along inter-QL neighboring planes.[14,21–23]

Defects such as vacancies, dislocations, and interfaces are structural features that interrupt the crystal lattice periodicity, but they can significantly modify the physical and optoelectronic properties. In 2D transition metal dichalcogenides, defects are specifically used for band gap engineering of the crystal.[24,25] Among defects, vacancies are of particular interest since they can act as quantum emitters with an impactful role on enhancing the quantum efficiencies for various optical quantum computation and sensing applications. Negatively charged nitrogen-vacancy (NV) centers in diamond[26] and hexagonal boron nitride (hBN)[27,28] are two examples of how vacancies can significantly contribute to enhanced optical properties of the crystal.

Hollow nanostructures, as nanostructures with large clusters of vacancies, have been found to exhibit promising plasmonic enhancement in comparison to their solid counterpart in noble metals-based plasmonic nanostructures.[29] This enhancement originates from the open yet confined geometry of cavities and results in enhanced transmission and reduction in absorption.[30–33] These studies show various hollow nanostructures with different hole configurations, such as Au rectangular holes,[34] Ag circular cavities,[35] and Ag nanoslits,[36] hold promise as building blocks in a wide range of applications from nanoscale sensors to wavelength filters for complementary metal-oxide semiconductor applications.[30,33] Such hollow nanostructures also highlight the role of interfaces, where two dissimilar materials, in this case the empty space and the crystal, meet each other.

Defects can be categorized into intrinsic and extrinsic. While intrinsic defects, i.e., hollow cavities, can naturally form during the synthesis process, extrinsic defects can form by external stimuli such as irradiation, electric potential, and thermal stress.[24,37,38] With a near-atomically real-time observation capability, in situ scanning/transmission electron microscopy (S/TEM) serves as an advanced nanoprobe to manipulate and characterize defects including their stability and transition dynamics under extreme environments.

To correlate the microstructural dynamics with the plasmonic properties and compositional changes during sublimation, in situ S/TEM can be combined with TEM analytical capabilities including X-ray energy dispersive spectroscopy (XEDS) and monochromated electron energy loss spectroscopy (Mono-EELS). In particular, in situ S/TEM in combination with EELS can be utilized to spatially and energetically resolve various plasmonic resonances.[39–41] While a wide range of techniques including scattering scanning-type near optical microscopy (s-SNOM)[42,43] photon electron emission microscopy,[44] cathodoluminescence,[45,46] electron energy loss spectroscopy (EELS)[41,47–49] has previously been used to study the surface plasmon resonances (SPRs), here we choose high-resolution scanning transmission electron microscopy (STEM)-(mono) EELS to characterize plasmonic resonances. While each of these techniques offers unique capabilities, each comes with its own limitations as well. For instance, while s-SNOM provides a higher spectral resolution, it is limited in the spatial resolution when compared with EELS.[39,42,50] In contrast to s-SNOM, a sub-nanometer-converged electron probe in EELS can probe both surface and volume (bulk) plasmonic states[40,41] near the defects as small as few nanometers in size at both static and dynamic conditions, such as defect growth during structural transformation.

Here, using in situ S/TEM combined with monochromated EELS, we investigate the electron-driven defect-plasmon interaction and explore how intrinsic defects (pinholes) and thermally induced polygonal defects can modulate the localized plasmonic response of nanostructures in low-dimensional chalcogenide crystals. Mono-EELS spectral imaging has been carried out to map the nanoscale spatial distribution of various plasmon resonances in 2D Bi_2Te_3/Sb_2Te_3 with ≈0.15 eV energy resolution. The studied 2D Bi_2Te_3/Sb_2Te_3 in-plane heterostructures contains a sharp heterointerface between Bi_2Te_3 and Sb_2Te_3 that is formed under a multistep solvothermal synthesis process.[51] Investigating physical and chemical tuning pathways as potential toolkits for tuning the plasmonic resonances in 2D Bi_2Te_3/Sb_2Te_3 in-plane heterostructures, we demonstrate how defects, interfaces, and edges can modulate and selectively enhance the plasmon modes in addition to shifting and broadening their excitation energies at room temperature ranging from hundreds of milielectronvolts to a few electronvolts.

The role of defects on the plasmonic response of the flake is further explored by intentionally introducing polygonal extrinsic defects into the flakes through a thermal sublimation process during an in situ TEM annealing experiment. Singular value decomposition (SVD) is used as a mathematical tool to disentangle the spectral data and identify the individual spectral contributions of various corner, edge, and face modes. The experimental findings are further combined with electron-driven discrete dipole approximation (e-DDA) simulations. Our results suggest that 2D Bi_2Te_3/Sb_2Te_3 in-plane heterostructure flakes can serve as an emerging platform for integrated plasmonics, offering a wide range of tunability and design flexibility. In addition, defects as physical inclusions can highly impact the selective enhancement of SPRs through introducing a confined geometry with new interfaces and edges in the system.

Sb_2Te_3 and Bi_2Te_3 can both support SPRs, and the presence of SPRs in the visible range of the pristine Bi_2Te_3 nanoplates has been previously reported.[21,52] 2D Bi_2Te_3/Sb_2Te_3 as a multicomponent hybrid heterostructure can offer a diversity of plasmonic responses. This can originate from the varying chemical composition along the heterointerface. Therefore, chemical modification of these hybrid nanostructures is a potential pathway to modify the plasmonic response. Furthermore, a heterointerface offers energetically favorable sites for forming thermally induced defects. To our knowledge, this is the first time both chemical and physical alterations have been combined in low-dimensional chalcogenide heterostructures to explore the response beyond the Bi_2Te_3 pristine nanoplates for enhanced plasmonic applications. In addition, integration of new interfaces (heterointerface, voids, etc.) allows for the design of plasmonic devices with new architectures. Plasmonic nanovoid structures and nanostructures containing plasmonic cavities have been shown to offer a promising platform for a wide range of biomolecular sensing applications including the next-generation sequencing technologies and single molecule detection.

2. Results and Discussion

Figure 1 shows the TEM structural analysis on 2D Bi_2Te_3-Sb_2Te_3 in-plane heterostructure. Figure 1a shows a TEM image of the 2D Bi_2Te_3-Sb_2Te_3 in-plane heterostructure on a lacey carbon grid with Bi_2Te_3 on the inside and Sb_2Te_3 at the outside of the junction. The contrast in Figure 1a reveals the presence of bent contours originating from the strain in the sample. The strain-induced ripple like pattern has been previously reported in solvothermally processed Bi_2Te_3 nanoplates.[21,51] A magnified TEM image of marked rectangular region (Figure 1a) is presented in Figure 1b, displaying how bent contours originate from the proximity of Te nanorod (NR) core at the center of the flake. Electron diffraction pattern (EDP) of the entire flake along the [0001] direction shown in Figure 1c shows that the flakes are single crystalline. While the diffraction spots from Bi_2Te_3 and Sb_2Te_3 are overlapped, the extra spots marked with orange circles are associated with the Te nanorod from the same zone axis at the central part of the flake. A high angle annular dark field (HAADF)-STEM of a flake with intrinsic pinhole defects is presented in Figure 1d. The corresponding XEDS chemical composition maps of this flake in Figure 1e–g show the flakes to be composed of a Bi-rich core with pinhole defects and Sb-rich outer shell. All images presented in Figure 1 have been acquired under static conditions at room temperature (RT) and

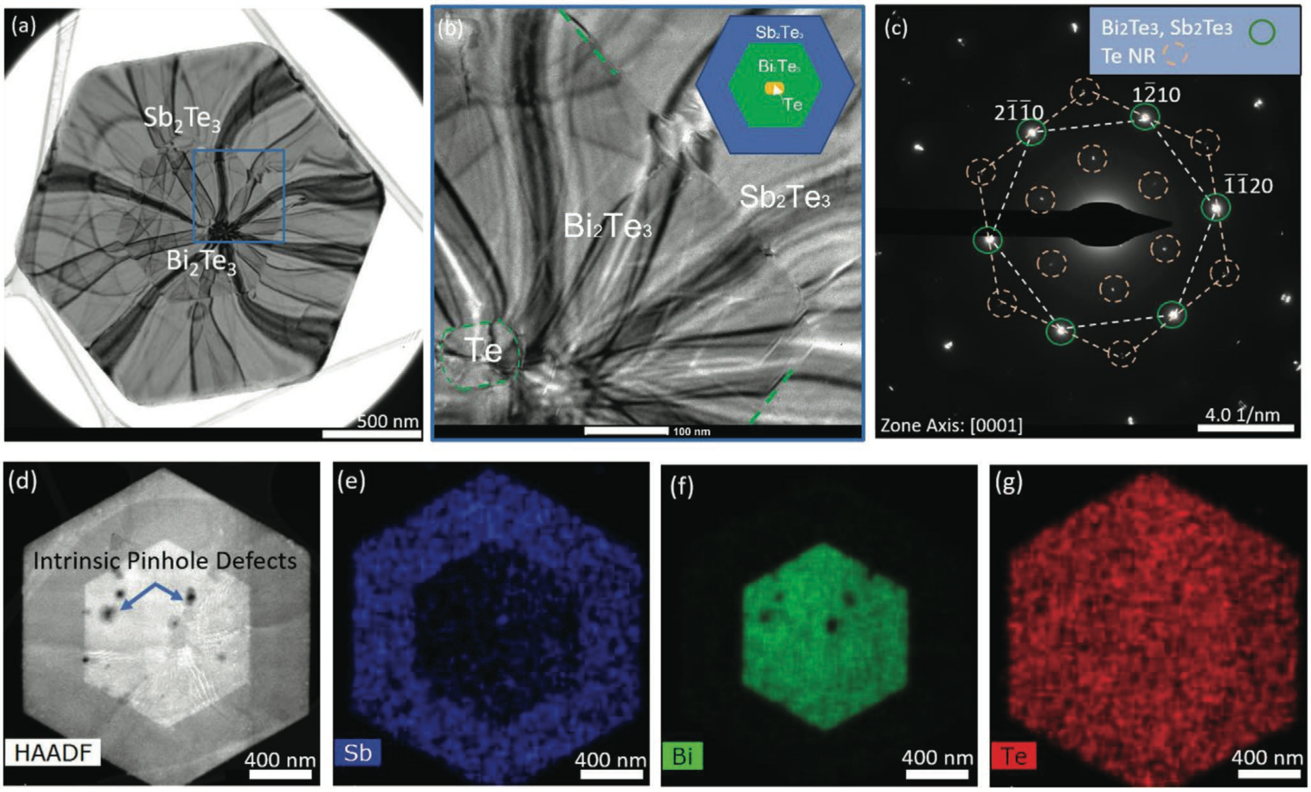

Figure 1. a) TEM image of interface area of Bi_2Te_3/Sb_2Te_3 in-plane heterostructures displaying bending contours. b) Magnified TEM image of marked rectangular area on a) displaying how bend contours origin from the neighboring area of Te nanorod. c) Electron diffraction pattern of the entire flake in (a) along [0001] direction exhibiting diffraction from Sb_2Te_3 and Bi_2Te_3 region and Te nanorod. d) Corresponding HAADF-STEM of the heterostructure containing intrinsic pinhole defects. e) Sb EDS chemical composition map confirming the composition of Sb_2Te_3. f) Bi EDS chemical composition map confirming the composition of Bi_2Te_3 region (Bi deficiency corresponding to defective regions). g) Te EDS chemical composition map confirming a relatively uniform distribution of Te atoms on both sides of the heterointerface.

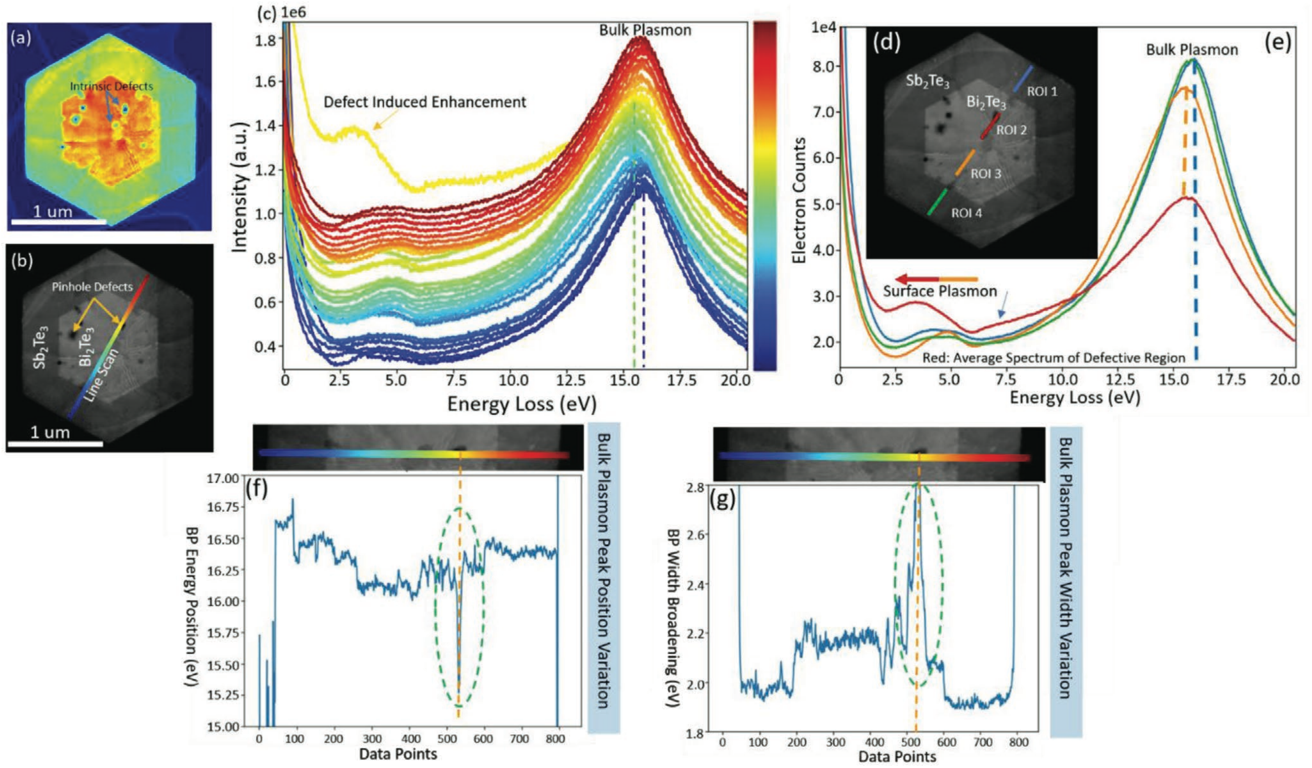

Figure 2. Modulation of plasmonic response in the presence of intrinsic pinhole defects. a) Jet colored TEM image of a Bi_2Te_3-Sb_2Te_3 in-plane heterostructure flake, highlighting the presence of intrinsic pinhole defects. b) Low-mag HAADF-STEM image of the Bi_2Te_3-Sb_2Te_3 in-plane heterostructure flake, displaying the area that the low-loss EELS spectra been acquired (passing through the intrinsic pinhole defects). c) Waterfall graph of the low-loss EELS line scan marked on (b) for every 25 spots in the original dataset, the distinct yellow spectrum corresponds to the one acquired from a pinhole defect. d) Average low-loss EELS spectra for ROIs 1–4 in which ROI 1 and 4 correspond to Sb_2Te_3 regions, ROI 2 and 3 correspond to Bi_2Te_3 regions. ROI 2 is from a region containing intrinsic defects (pinhole). e) Low-mag HAADF-STEM image of the Bi_2Te_3-Sb_2Te_3 in-plane heterostructure flake displaying the corresponding regions marked ROI (1–4) from which the average low-loss EELS spectra are plotted. f) Plot of bulk plasmon peak position variations by Gaussian fitting the bulk plasmon for 800 data points along the line scan displaying over 1.1 eV peak position shift toward lower energies (red shift) induced by intrinsic defects. g) Plot of bulk plasmon width variations by Gaussian fitting the bulk plasmon for 800 data points displaying over 0.7 eV defect-induced width broadening.

accelerating voltage of 80 kV. The XEDS chemical composition maps of the pristine (defect free) flake is presented in Figure S1 in the Supporting Information.

Pinhole defects are observed as intrinsic defects in these in-plane heterostructures. Intrinsic pinhole defects can mimic the response of a cluster of vacancies in the structure. To understand the effect of pinholes on the plasmonic response, plasmon resonances are studied through 1D spectrum imaging (line scan) EELS. **Figure 2**a shows a jet color map of the pinhole defects scattered within Bi_2Te_3 over lacy carbon. A line scan EELS over the pin hole defects and across the flake with 5 nm step size containing ≈800 data points is performed in the STEM mode (Figure 2b,c). Figure 2b shows an HAADF-STEM image with a 1D line scan spectrum image passing across the flake. Figure 2c shows the low-loss EELS spectrum stacks corresponding to data points along the line scan with every 25th spectrum present in the graph. The distinct yellow spectrum corresponds to the vicinity of a pin-hole defect with an enhanced surface-plasmon response in the visible-UV regime. This spectrum shows a dominant surface plasmon mode at ≈3 eV. The spectra corresponding to defect-free region show a dominant peak centered around ≈16 eV corresponding to the bulk plasmon resonance of Bi_2Te_3 and Sb_2Te_3. A small chemically induced blue shift to higher energies in the bulk plasmon response is observed between Bi_2Te_3 and Sb_2Te_3. This blue shift is due the chemical composition variation across the interface. The bulk plasmon peak in Sb_2Te_3, Bi_2Te_3 based materials has been consistently observed and reported via EELS. The resolved bulk plasmon peak position is consistent with previous measurements.[19,20,53–55]

The bulk plasmon resonances originate from the bulk response in Bi_2Te_3 and Sb_2Te_3. The bulk (volume) plasmon energy changes due to the density of valence electrons in insulators and semiconductors. Bulk plasmons correspond to longitudinal waves and are the electron oscillations relative to the positive ion cores. In EELS, using fast electrons as an excitation source, we can excite and probe the bulk plasmon resonances in a geometry where the probe penetrates the sample.[56]

To further explore and quantify the possible effect of intrinsic defects on the plasmonic response, the line scan is sectioned into four segments, region of interest (ROI) (1–4), with each segment consisting of 120 data points along the Bi_2Te_3 and Sb_2Te_3 regions (Figure 2d). ROI 1 and 4 are both from Sb_2Te_3 while ROI 2 and 3 are from Bi_2Te_3 and share the same chemical composition. The average plasmonic response of data points for each ROI is plotted in Figure 2e. At the vicinity of the pinhole in ROI 2 with a defect, the broad surface plasmon peak is red shifted and the surface to bulk plasmon ratio is highly increased compared to the other segments. An obvious red shift to lower energies as well as broadening is also observed in the bulk plasmon peak in ROI 2. ROI2 and ROI3 have the same chemical composition, therefore, any shift or broadening should be attributed to morphological changes such as presence of defects or strain. The enhanced surface to bulk plasmon ratio at the vicinity of the defects is due to the presence of a higher surface area as well as the nanoscale cavity with enhanced transmission. In addition, we observe a small broad peak (Figure 2e, shown by blue arrow) that is enhanced in the defective region of Bi_2Te_3 (ROI2). This peak could be attributed to either excitation of a new surface plasmon mode (between 5 and 7 eV) or significant enhancement of an existing mode that is heavily suppressed in the defect-free region of Bi_2Te_3. It is worth noting that these broad surface plasmon features may also consist of multiple surface plasmon modes too close in energy to be resolved distinctly due to our limited spectral resolution.

To quantify how defects modulate the energy and width of the bulk plasmon peak, we did Gaussian fitting for the bulk plasmon peaks. Figure 2f shows the bulk plasmon energies corresponding to all data points along the line scan (marked on Figure 2b). A drastic red shift of over 1.1 eV is observed in the bulk plasmon energy at the vicinity of the pinhole defect compared to defect-free areas in Bi_2Te_3 region. The bulk plasmon mode is red shifted to as low as ≈15.25 eV in vicinity of the defect.

Furthermore, the bulk plasmon peaks width across the line scan is quantified and plotted in Figure 2g. Peak broadening of around ≈0.7 eV is observed across the line scan with the broadest bulk plasmon peak corresponding to the defective region (pinhole intrinsic defect). Our observations highlight how defects and morphological changes can significantly modulate the local plasmonic response, observed as peak shift and broadening. These observations suggest strong hybridization between inner and outer electric field leading to the enhancement of the local electric field at the vicinity of the defects. In addition, the small local fluctuations in bulk plasmon energy in the area with same chemical composition (observed in Figure 2e,g) can arise from strain or impurities. Strain can potentially induce a small local change in lattice parameter and modulate the density of valence electrons, which can cause a slight shift in the plasmon peak as previously observed.[57]

Controlled introduction of the defects into the structure can be a powerful tool to optimize a targeted plasmonic response and can be a promising route toward nanopore plasmonic devices.[24] In addition, understanding the underlying physics behind the formation and growth process of the defects is of utmost importance. Using in situ S/TEM heating, we have successfully induced facetted polygonal defects within the Bi_2Te_3/Sb_2Te_3 heterostructure. The induced defects start to appear in 2D Bi_2Te_3/Sb_2Te_3 flake at about 300 to 370 °C by a constant heating rate of 5 °C min^{-1} under vacuum with no chemical agent. Figure S2 in the Supporting Information shows pristine 2D Bi_2Te_3/Sb_2Te_3 heterostructures on the in situ heating device at RT before annealing. Figure S3 in the Supporting Information displays the formation and growth of polygonal defects in the 2D Bi_2Te_3/Sb_2Te_3 heterostructures with preferential sublimation along prismatic $\{1\bar{1}00\}$ planes. Here by thermally induced defects, we are referring to thermally induced nanopores (cavities). The polygonal nanopores form as the materials sublime and leave a materials deficient region which appears with white contrast in **Figure 3**a and Figure S3 in the Supporting Information. Figure S4 in the Supporting Information shows the XEDS of a Bi_2Te_3/Sb_2Te_3 flake during sublimation indicating the chalcogenide (Te) depletion. The details on the mechanism behind the sublimation and growth of the defects under annealing are beyond the scope of this work and are presented in a separate paper.

To understand the impact of these thermally induced defects, 1D low-loss EELS spectrum imaging is carried out during in situ heating of the sample. Figure 3a shows an STEM image of the flake at ≈330 °C displaying the EELS line scan location. To understand how the surface plasmon modes evolve at the vicinity of the defects, the 2D EELS line scan plot is extracted and presented in jet color map in Figure 3b along with the observed polygonal defect in Figure 3a. The blue regions correspond to lack of signal from the Bi_2Te_3 bulk plasmon resonance inside the defect (it is marked in Figure 3c). The data presented in Figure 3d–g are focused on the defect 2 (marked with a white circle inside Bi_2Te_3 region). Figure 3d shows a magnified image of defect 2. Three segments of the line scan corresponding to upper edge (blue), middle (orange), and lower edge (green) are marked in Figure 3d. Figure 3e displays the three average spectra corresponding to segments 1–3 in Figure 3d. An enhanced surface plasmon response for spectra 1 and 3 which corresponds to the edge modes is observed. In addition, the ratio of surface to bulk plasmon is increased at the edge in comparison to what we observed in Figure 2c for intrinsic defects. In other words, the bulk response at the edges of the defect is highly suppressed, while the surface plasmon response becomes dominant. Eventually, the surface response decays as the electron beam moves away from the edge of the defect toward the center as is shown for region 2 in Figure 3d. Looking at spectrum 2 at the center of the defect, the electron beam does not sense the surrounding environment and the very subtle and broad bump likely arises from the ultrathin amorphous carbon underneath the flake.

To further probe how the edges contribute to the plasmon excitation, we probe the surface plasmon excitation at the vicinity of the defect edge in consecutive spot scans. Figure 3f,g shows a magnified image of defect 2 with a few consecutive probe positions and the EELS spectra associated with each point. At the defect edge, the surface plasmon peak 1 is red shifted to lower energies. In addition, the surface plasmon peak 2 (marked with circle) starts to dominate at the defect edge potentially indicating an excitation of a new surface plasmon from a strong hybridization of inner and outer electromagnetic field at the defect edge. Beside the modulations in the surface plasmon modes, the bulk response is also suppressed and nearly disappearing right on the edge of the defect. These observations strongly suggest that the induced polygonal defects can be a promising tool for tuning the plasmonic response in 2D Bi_2Te_3/Sb_2Te_3 in-plane heterostructures.

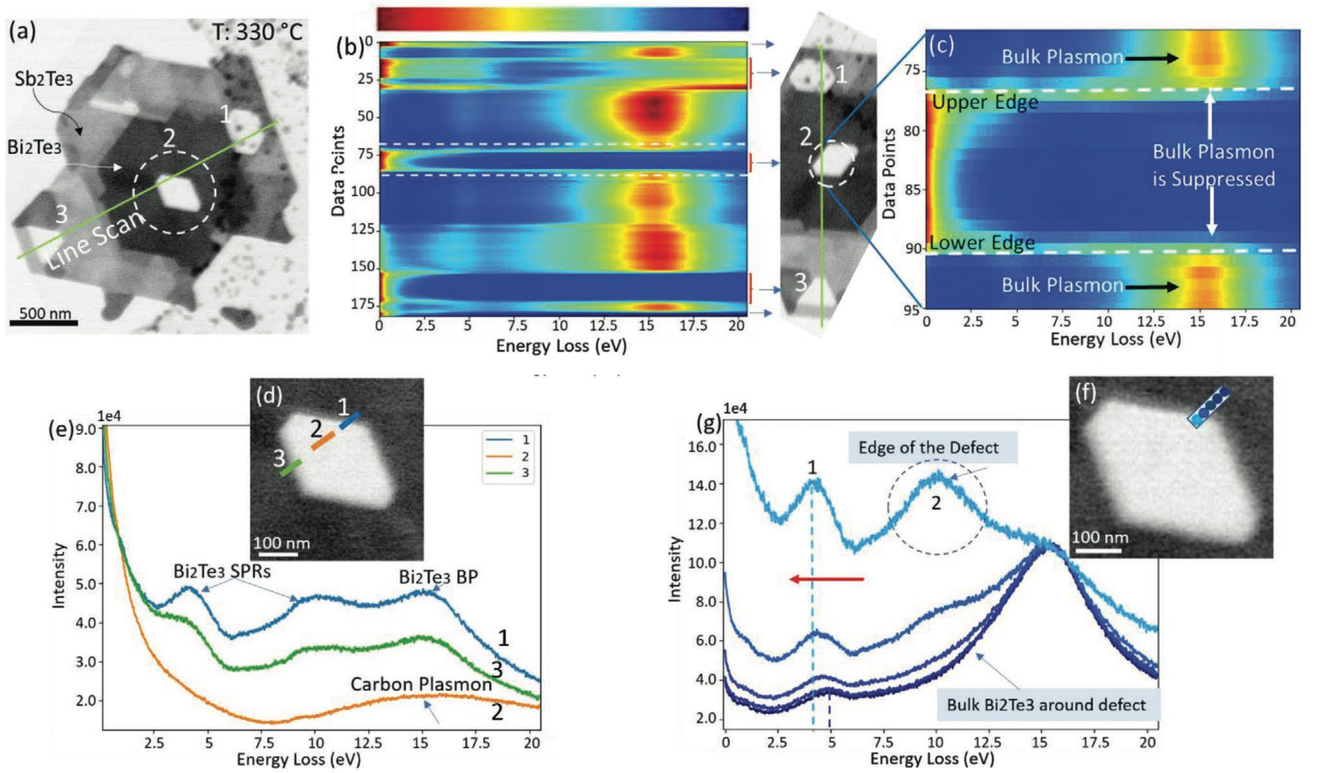

Figure 3. Plasmonic variations induced by an extrinsic polygonal defect. a) Formation of extrinsic/thermally induced polygonal defects at ≈330 °C in Bi_2Te_3-Sb_2Te_3 in-plane heterostructure. Green line corresponds to the low-loss line scan EELS. b) 2D plot of line-scan spectra in jet color map. Dark regions correspond to lack of bulk plasmon signal therefore where defects are located, c) a zoomed-in 2D line scan plot acts as a road map to precisely identify the data points corresponding to the defect edge/border of defect 2 (central defect inside Bi_2Te_3 region). d) Magnified image of defect 2 showing three segment of the line scan across the defect (1–3). e) Three averaged low loss EELS spectra acquired from marked segments on (d) corresponding to the upper edge, middle, and lower edge of the defect (the upper edge and lower edge for defect 2 is marked by dashed line in (c). f) Magnified image of defect 2 displaying the five consecutive locations across the upper edge of defect. g) Five consecutive low loss EELS spectra corresponding to the marked point on the defect.

While intrinsic and extrinsic defects can have a profound effect on the plasmonic resonance of nanostructures, edges and interfaces in nanostructures can also modulate the plasmon resonances. **Figure 4** shows how plasmonic resonances could be modulated at the heterointerface (between Bi_2Te_3 and Sb_2Te_3) and the edges in a nanostructure. Figure 4a shows three assigned ROIs (0–2) corresponding to Bi_2Te_3, Sb_2Te_3, and their heterointerface. Figure 4b–d displays the SPRs below 8 eV and the bulk plasmon peak around 16 eV. A blue shift of ≈0.4 eV to higher energies is observed in bulk plasmon originating from chemical composition variation as the electron probe moves from Bi_2Te_3 to Sb_2Te_3. The bulk plasmon peak energy for the heterointerface region 1 is in the middle of the bulk plasmon energy range as both Bi_2Te_3 and Sb_2Te_3 are probed in this measurement. This is a confirmation that the observed shift in bulk plasmon peak position originates from variations in chemical composition across the interface.

Figure 4d shows modulations in the surface plasmons with composition. A red shift to lower energies is observed in surface plasmon excitations as the electron probe moves into Sb_2Te_3. In addition to a red shift of about 0.35 eV, the lower energy plasmon mode in Sb_2Te_3 is significantly enhanced compared to the other two spectra. This shift and enhancement can have a mixed nature of chemical, geometrical, and morphological origin due to having a different size as well as being closer to the flake edge. Overall, the plasmon peak position and ratio variations indicate that heterointerfaces can potentially offer another way to tunability and flexibility for Bi_2Te_3/Sb_2Te_3 in comparison to Bi_2Te_3 hexagonal flakes reported previously.[21]

Our experimental observations show defects and heterointerfaces to have profound effects on the surface plasmon excitations in Bi_2Te_3/Sb_2Te_3 in-plane heterostructures. To spatially resolve the distribution of various plasmon resonances, a 2D low-loss EEL spectrum image is acquired from the marked region in Figure 4e. Figure 4f–n shows selected series of 2D low-loss EELS maps acquired at indicated energies with an energy window of (0.4 eV). These 2D EELS maps highlight the spatial distribution of the plasmon resonances corresponding to the observed peaks (intensity amplitude for each pixel position in the 2D spectrum image). Edge- and face-localized surface plasmon modes are the dominant resonances observed in Figure 4. Edge-localized modes are mainly excited at a lower energy range, while face-localized modes are excited at higher energies. Although there are similarities in the corresponding spatial distribution maps of face-localized and bulk plasmon mode, these modes are fundamentally different from each other since they are excited at very different energies. Movie S1a in the Supporting Information plays the sequential frames

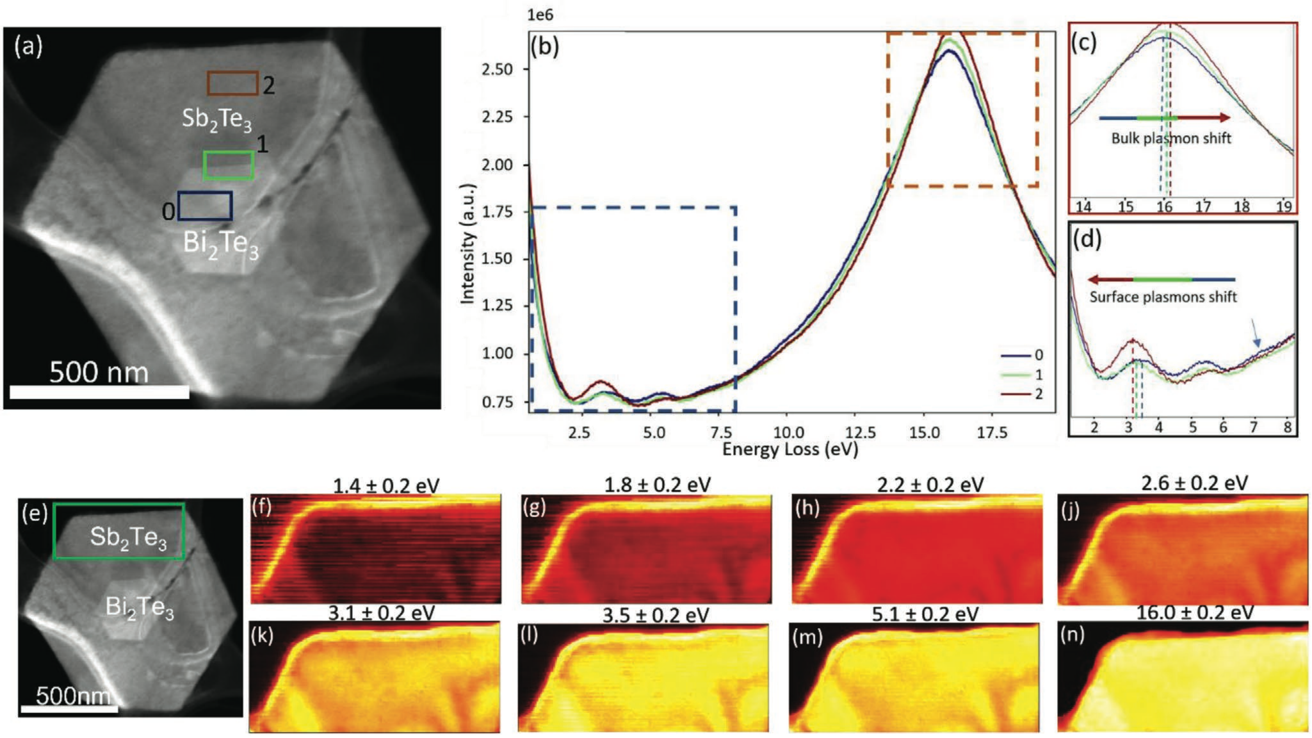

Figure 4. Plasmons modulation by the presence of a heterointerface and spatial distribution of SPR modes. a) HAADF-STEM of Bi_2Te_3-Sb_2Te_3 heterojunction displaying the 3 ROI (0–2) from where the spectra in (b) is acquired, ROI0: Bi_2Te_3, ROI1: heterointerface, ROI2: Sb_2Te_3. b) Low-loss EELS spectra corresponding to ROI (0–2), exhibiting a shift in both SPR and BP as the electron probe moves from Bi_2Te_3 region to Sb_2Te_3. Plasmon energy shift in both sides of the junction. c) Magnified low-loss EELS spectra displaying the chemical composition-induced shift in the bulk plasmon resonance. d) Magnified low-loss EELS spectra displaying the red shift in SPR energy as the electron probe moves into Sb_2Te_3. e) Low-mag HAADF-STEM displaying where the 2D EELS spectrum images are acquired (green rectangle). f–n) 2D EELS map acquired using an energy window of 0.4 eV, exhibiting the spatial origin and distribution of various electronic excitations including SPR and BP, the SPR modes displaying two major spatial distribution with edge modes dominating the lower energy range excitations and face modes dominating the beyond visible range (UV regime) excitations.

of the real space 2D EELS maps (intensity maps) acquired from the top corner of the flake for energy losses below 20 eV. As the energy navigator moves along the energy loss axis on the average low-loss spectrum (Movie S 1b, Supporting Information), the transition from edge-localized modes to face-localized and finally to bulk plasmon mode can be observed. Here, we mainly observe edge, face, and bulk plasmon resonances, since the individual plasmon peaks are too close to each other overlapping in the energy space and cannot be resolved individually with our experimental energy resolution.

To reduce the noise and dimensionality of the data and further deconvolute the surface plasmon modes and the overlapping features of the spectrum, we apply SVD to resolve various plasmonic resonances.[58–61] SVD analysis was carried out to the dataset in Figure 4 to assess various spectral contributions in the spectrum images and the resulting deconvoluted resonance maps are presented in **Figure 5**b–h. Figure 5j,k shows the *S* and *U* components of the SVD analysis. *U* contains the singular vectors with the highest intensity, each representing a basis spectrum present in the data, while *S* contains the singular values that encode the weighting of each component. In addition, *V* contains the right singular vectors that hold the amplitude of the spectra at a given pixel number and can be reshaped to x,y as a 2D image. Among the first ten SVD components, the first seven seem to contain physical information which is shown as the intensity variation maps in Figure 5b–h. The intensity maps are the 2D images of the reshaped right singular vectors V and display the spatial origin of the first even components resulting from the SVD.

The 2D maps presented in Figure 5b–h can be compared to the 2D EELS maps presented in Figure 4. SVD components 1 and 2 in Figure 5b,c present plasmon resonance modes similar to the 2D EELS maps for the surface (face mode) and bulk plasmons. These two modes are the first two major components mainly describing the bulk and face-localized response out of the seven significant SVD components. Components 3–7 show significant variations along the edges and boundaries. Among them, components 3, 5, and 7 all display edge intensity enhancement corresponding to dissimilar SPRs (edge modes). For example, components 3 and 5 show the surface plasmon edge mode maps corresponding to the energy range of 1.2–1.6 and 2.4–2.8 eV, respectively. In contrast, component 4 displays a corner-localized intensity enhancement which is due to the presence of a corner-localized plasmonic mode in the structure. This mode is not revealed in the pristine 2D EELS maps in Figure 4, most likely due to the noise and the possibility of having low energy hidden under the tail of the zero-loss peak (ZLP). The intensity maps for components 8–10 (Figure S5 in the Supporting Information) do not hold any significant physical information about the structure and the intensity

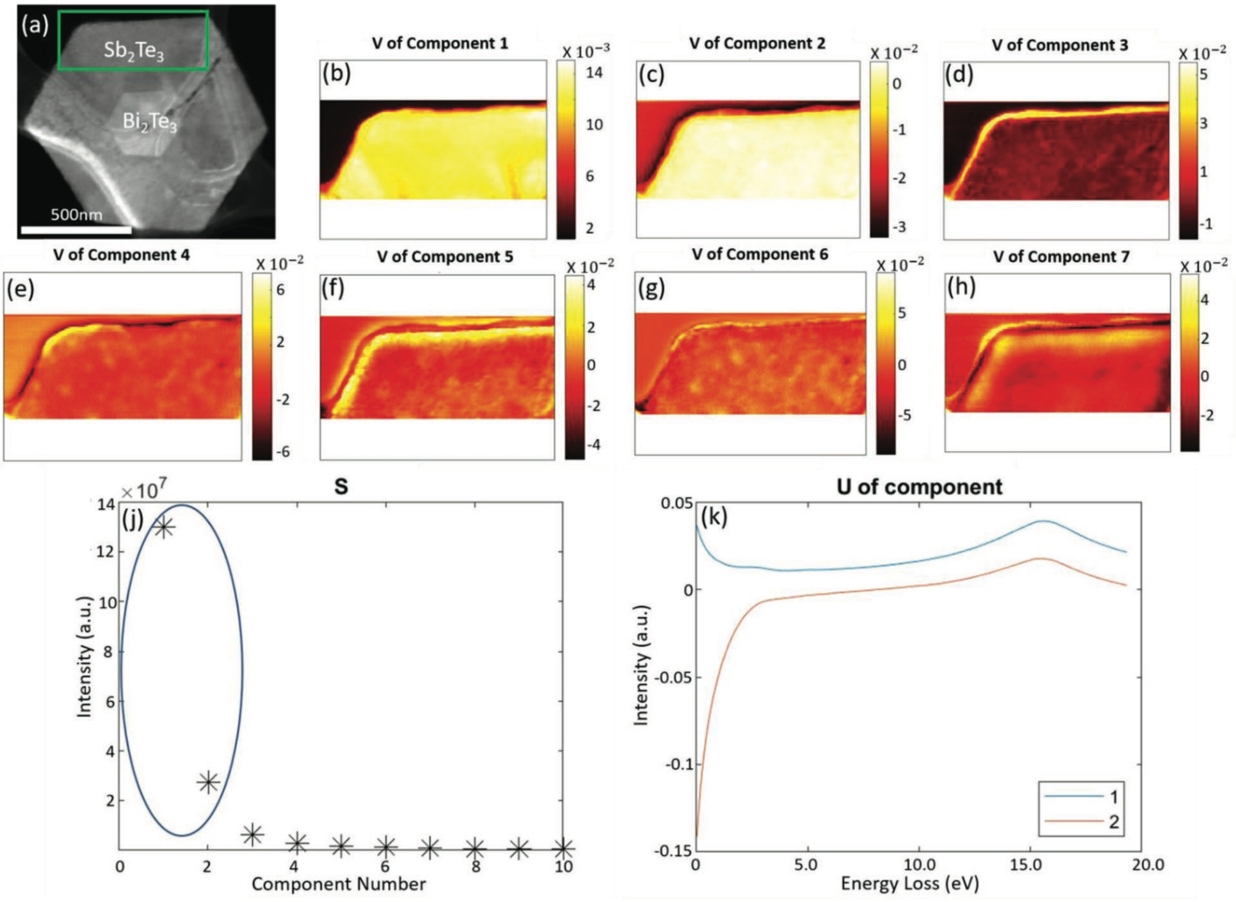

Figure 5. SVD analysis to assess various spectral contributions. SVD components from the dataset acquired from the ROI in (a). b–h) Right singular vectors, *V*, for component (1–7) indicating the spatial origin of *U*(:,ii), the right singular vectors contain the amplitude at a given pixel number and can thereby be reshaped to *x*,*y*. j) *S*(ii,ii), the singular values contain the weighting, k) *U*(:,ii), the left singular vectors contain the spectra for the first two dominant components.

variation is most likely due to the noise in the original datacube. By edge mode or corner mode, we are particularly referring to the spatial distribution of the localized surface plasmon modes. Corner, edge, and face modes are transverse modes and the term edge, corner, face, etc., only refers to the spatial localization characteristics of the spectrally probed SPRs.

Both the SVD analysis and the 2D EELS maps indicate good agreement for the various SPRs at different energy losses. While the experimental 2D maps present all the modes, SVD analysis deconvolutes dissimilar edge and corner modes among the SPRs observed here. This analysis further shows how the morphology and geometry of the flakes can give rise to a wide range of dissimilar and complementary SPRs within the energy space.

Finally, e-DDA simulations are performed to qualitatively support the experimental results and illuminate the underlying modes that give rise to the spectra of both the Bi_2Te_3 and Sb_2Te_3 hexagonal flakes. The simulation details and parameters are included in the Experimental Section. **Figure 6**a displays simulated aloof beam EEL spectra for both Bi_2Te_3 and Sb_2Te_3 flake (the electron beam is located outside of the flake) to compare the plasmonic responses of Bi_2Te_3 and Sb_2Te_3. A clear redshift of the surface plasmon modes to lower energies is observed moving from Bi_2Te_3 to Sb_2Te_3 which is in accordance with the experimental observations in Figure 4,i. Figure 6b presents EEL spectra for Sb_2Te_3 under various electron beam configurations relative to the flake (perpendicular vs parallel). As evident from Figure 6b, various plasmonic modes can be excited by varying the electron beam orientation relative to the flake.

An electron trajectory that runs parallel to the hexagon plane can drive not only the corner- and edge-localized surface plasmon modes, but also the various face-localized plasmons. The face-contained modes are less evident when using an electron probe with a trajectory perpendicular to the hexagon plane (the same trajectory used in experimental data) as explicitly shown by Figure 6b. The first and second peaks in the EEL spectrum of Figure 6a,b correspond to the corner-localized dipole and quadrupole modes of the hexagon nanoparticles, respectively. As the energy increases, the modes evolve from corner-localized (3.5–5.5 eV) to edge (≈6 eV) and further into face-localized modes (7–10 eV). The comparison of electron beam trajectories was made with the Sb_2Te_3 dielectric material; based upon Figure 6a, these peaks would be expected to blue shift if the Bi_2Te_3 dielectric material is used instead. The unique

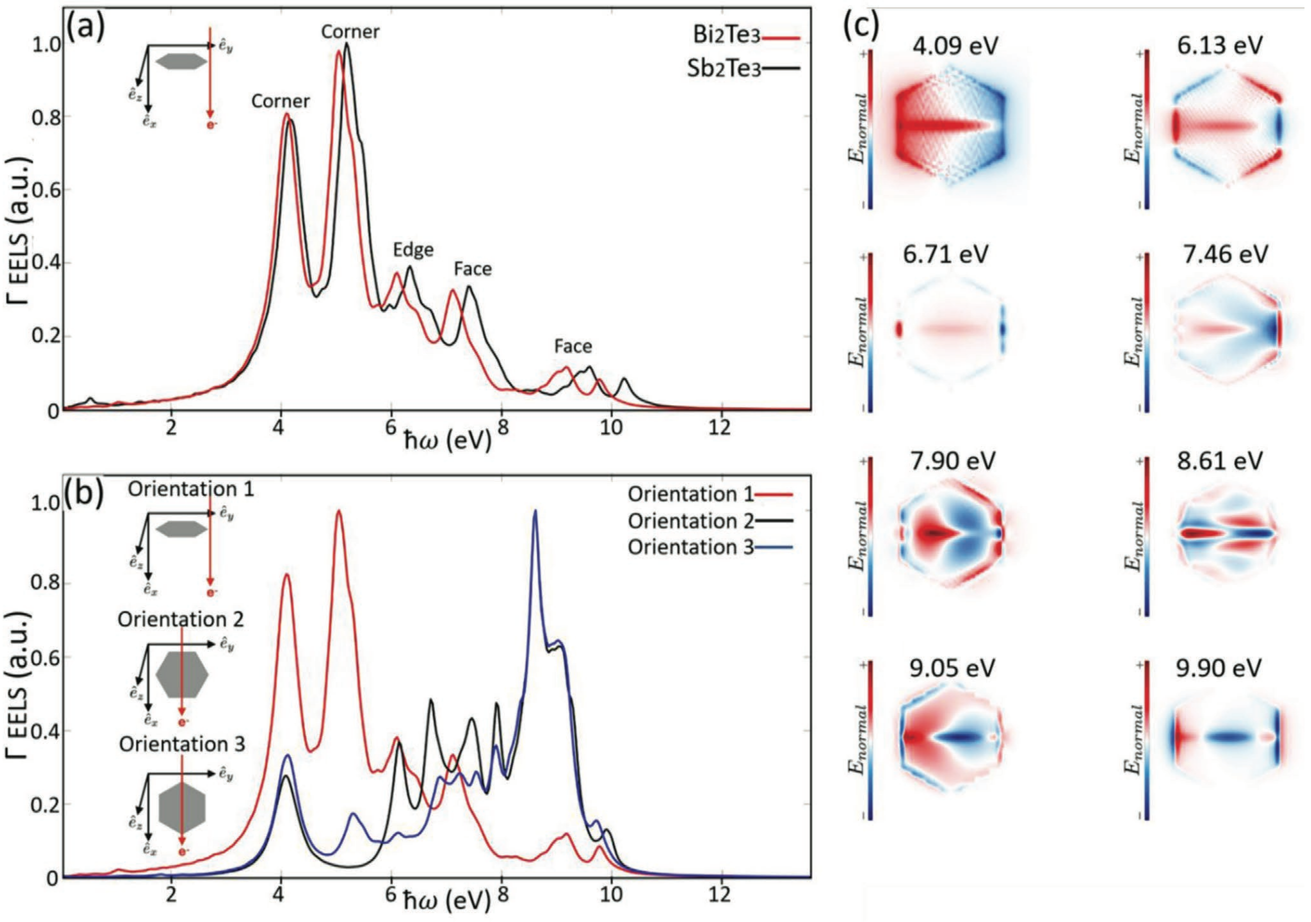

Figure 6. Simulated EEL spectra and plasmonic electric field profiles. a) Simulated EEL spectra under an aloof beam trajectory oriented perpendicular to a Bi_2Te_3 and Sb_2Te_3 flake displaying a red shift in the SPR between Bi_2Te_3 and Sb_2Te_3. b) Simulated EEL spectra under three different aloof beam trajectories with the higher-order modes enhanced under the two parallel beam geometries (black, blue). c) Corresponding plasmonic electric field profiles of various surface plasmon modes displayed in (a) with the lower-order modes (i.e., the lowest energy modes) corresponding to edge and corner localized surface plasmons and the higher-order modes (i.e., the highest energy modes) corresponding to face localized surface plasmons. In all cases, the electric field component normal the flake is displayed and is proportional to the surface charge density of the plasmon mode at that resonance energy.

TI plasmonic modes of the hexagon flakes are visualized by the electric field maps displayed in Figure 6c. These maps shows electric field profiles of various surface plasmon modes displayed in (a) with the lower-order modes (i.e., the lowest energy modes) corresponding to edge- and corner-localized surface plasmons and the higher-order modes (i.e., the highest energy modes) corresponding to face-localized surface plasmons. In all cases, the electric field component normal the flake is displayed and is proportional to the surface charge density of the plasmon mode at that resonance energy. These maps show the normal component of the electric field relative to the flake surface. The surface plasmon peaks on the simulated spectra are narrower and easily distinguishable from one another in comparison with broad surface plasmon peaks that we observed in the experimental EEL. The damping parameter (γ) in the Durde–Lorentz model can play a significant role on the peak width (narrow peaks in simulated results vs broad peaks in experimental results). A comparison between simulated data and adapted experimental data[1,9,21] is shown in Figure S6 in the Supporting Information. In the simulated spectra shown in Figure 6a,b, the damping parameter is reduced by an order of magnitude ($\gamma \mapsto \gamma/10$). The experimental data converge well with the simulated data for higher damping parameter as shown in Figure S6 in the Supporting Information. Damping parameter increases as a function of internal collision and scattering events (losses). The presence of defects and strain in the flakes are the major contributor for increasing scattering events therefore higher damping rate and broader surface plasmon peaks on the EEL spectra.

3. Conclusions

Our results demonstrate the promising plasmonic properties of 2D Bi_2Te_3-Sb_2Te_3 in-plane heterostructures, particularly their wide spectral tunability range. Various SPRs in the UV-vis range with varying spatial distributions including corner-, edge-, and face-localized modes were identified and resolved using STEM-EELS spectrum imaging combined with SVD analysis. Two types of defects (extrinsic and intrinsic) have been explored as potential tools to tune the plasmonic responses in the 2D Bi_2Te_3/Sb_2Te_3 in-plane heterostructures. In addition, we show the presence of heterointerfaces and defects can be used as pathways to tune and manipulate plasmonic responses over a broad energy range. In situ TEM is further shown as an effective tool for thermally inducing controlled defects in this structure. Companion e-DDA simulations further identify the nature of the plasmonic modes and their corresponding spatial distributions. e-DDA simulations highlight the impact of electron trajectory on selective enhancement of lower-energy SPRs (corner modes) versus higher energy modes (edge and face modes), therefore, a potential pathway for exploring in future studies.

4. Experimental Section

Preparation of Bi_2Te_3/Sb_2Te_3 In-Plane Heterostructure: Hexagonal 2D Bi_2Te_3 nanoplates were synthesized via a solvothermal process and using tellurium oxide (TeO_2) and bismuth oxide (Bi_2O_3) in the stoichiometry ratio at 180 °C. Primarily a solution out of 0.48 g of polyvinylpyrrolidone and 30 mL ethylene glycol was made at 100 °C. 15×10^{-3} M sodium hydroxide (NaOH), 1.7×10^{-3} M tellurium oxide (TeO_2), and 0.6×10^{-3} M bismuth oxide (Bi_2O_3) were added to the solution and stirred continuously till the dispersed solution was acquired. The solution was then transferred and maintained at 180 °C for 15 h. A schematic of Bi_2Te_3 nanosheets from Te nanorods is shown in Figure S7 in the Supporting Information. The material was then washed with water several times and freeze-dried to prevent oxidation and kept in argon-filled glovebox afterward. For Bi_2Te_3/Sb_2Te_3 heterostructure synthesis, after Bi_2Te_3 nanosheets were produced and washed they were loaded back, and a second synthesis step took place by having Sb_2O_3 and TeO_2 as precursors to make the growth of Sb_2Te_3 as an outer junction took place from the edges of 2D Bi_2Te_3 nanosheets section.[23,62]

Characterization (Instrumentation and Data Acquisition): TEM samples for 2D Bi_2Te_3/Sb_2Te_3 in-plane heterostructure were prepared using solvent-assisted exfoliation (a 1:1 mixture of isopropyl alcohol and deionized water) following 30–45 min of sonication to acquire a clear solution. A drop of the clear solution was dropped over a TEM lacey carbon grid and left to become dried. Talos F200X scanning/transmission electron microscope with a super XEDS detector at accelerating voltage of 80 kV was used to acquire HAADF- STEM images and XEDS maps. To remove contamination, the samples were beam showered for approximately an hour in TEM mode at a low magnification before switching to the STEM mode. The STEM-EELS data and in situ TEM data were acquired using a double aberration corrected Titan equipped with a Gatan GIF and a monochromater, operating at accelerating voltage of 80 kV and spot size 14 with energy resolution of ≈0.14 eV under a dual EELS condition. During STEM-EELS data acquisition, a C3 aperture of 50 um and a C2 aperture of 150 ums were used. Spectrum imaging (SI) data were collected using a focused rastering probe over a 2D ROI or 1D ROI (line scan) of several hundred nanometers and acquiring electron energy loss spectra at every pixel resulting in a 3D dataset (for the case of 2D spectrum image) and 2D dataset (in case of 1D line scan). The electron probe current was set between 80 and 120 pA. Gatan-GIF aperture size of 2.5 mm, energy dispersion of 0.025 eV Ch^{-1}, dwell time of 10 ms for each spectrum were used during SI data acquisition. SI multi-dimensional datasets were analyzed using Hyperspy, an open-source Python software package.[63] Sequential frames (movies) were made using interactive functions between signal space and image space (x,y) acquired during SI acquisition.

Spectral Processing: Data analysis was performed on hyperspectral images mainly using Hyperspy,[63] an open-source Python software package combined with various other Python libraries including Numpy, Matplotlib, and Scipy. Using Hyperspy, all spectra were aligned according to their ZLP maximum position (finding the maximum between ±1 eV) and setting the new position to zero. The energy axis was then calibrated using cross-correlation between low-loss spectra (ZLP) and high-loss spectra in dual-EELS. Multiple interactive functions were implemented in Hyperspy allowing direct comparison between plasmonic response of several ROIs and to observe the plasmonic dynamic in the structure in a more intuitive way. Experimental 2D-EELS maps were also normalized to the same maximum for better visibility.[64]

SVD Analysis: A benefit of noise-free synthetic data was in the clear visibility of the data variation among given latent factors. The introduction of noise was resulted in smearing of the underlying spectral compositions such that the only dominant variation trends were visible.[58,61]

Singular value decomposition is a method of decomposing a 2D dataset into a series of significant basis vectors. In this case, the acquired 3D datacube from spectrum imaging could be reshaped into a 2D dataset (spectrum, pixel). The resulting matrix was then decomposed into its singular vectors: three matrices consisting of two orthogonal matrices containing the basis spectra and one diagonal matrix as shown below

$$A = USV^T \tag{1}$$

In which A is the original 2D matrix (m_{Spectra} x n_{pixels}) and it decomposes into U (an m x m matrix), S (an $m \times n$ diagonal matrix), and V ($n \times n$ orthogonal matrix). In the case of the partial SVD, only the first i components were calculated, in which case the U, S, and V simplified to a series of i vectors and values. By taking the first i significant SVD components of a dataset, it was possible to reduce the rank and noise of the dataset as the SVD components were calculated in the order they contributed to the dataset since the actual spectra appeared in the first components where the noise or minor artifacts and fluctuations were present in later components.[58–60]

EELS Simulation: Numerical EEL simulations were performed with the electron-driven discrete dipole approximation (e-DDA) package.[65,66] This package utilized the familiar coupled dipole approach of DDA, but with the exciting field of a swift electron as the probe instead of the optical field. Here, e-DDA was used to analyze the plasmon modes of the hexagon nanostructures considered in this experiment, however, the simulated hexagons were scaled down in size to facilitate numerical convergence. The hexagon flakes used for simulation had a thickness of 10 nm and width of 50 nm and were taken to be in vacuum. A high discretization (1 nm dipole spacing) was used, and the primary electron beam kinetic energy for all simulations was 60 keV. The impact parameter was 2 nm for all simulations. Electron beam-induced electric fields were calculated on a plane parallel to the hexagon face, 1 nm off the surface of the nanoparticle. The dielectric constants used for simulation were obtained from fitting a Drude–Lorentz model to the dielectric constants of both Bi_2Te_3 and Sb_2Te_3 given by Yin et al.[9]

To best capture the plasmonic response of the hexagonal flakes, the dielectric functions of both Bi_2Te_3 and Sb_2Te_3 were fit to a Drude–Lorentz model. The radiative damping of the Drude–Lorentz oscillator, for both Bi_2Te_3 and Sb_2Te_3, was decreased by an order of magnitude to narrow the linewidths of the various peaks so a distinction could be made between the many corner-, edge-, and face-localized modes. The process of using a dielectric function fit allowed for an appropriate qualitative comparison between experiment and simulation, while also offering insight into the many plasmonic modes of the system.

Based on the Drude–Lorentz model $\varepsilon(\omega) = \varepsilon_\infty + \dfrac{\omega_p^2}{\omega_0^2 - \omega^2 - i\omega\gamma}$, the dielectric parameters for Bi_2Te_3 and Sb_2Te_3 are as follows[9]

Bi_2Te_3: $\varepsilon_\infty = 1$, $\hbar\,\omega_p = 12.4$ eV, $\hbar\,\omega_0 = 1.75$ eV, $\hbar\gamma = 0.14$ eV,
Sb_2Te_3: $\varepsilon_\infty = 1$, $\hbar\,\omega_p = 11.8$ eV, $\hbar\,\omega_0 = 1.90$ eV, $\hbar\gamma = 0.16$ eV.

The computed bulk plasmon energies using the Drude–Lorentz model for Bi_2Te_3 and Sb_2Te_3 were 12.52 and 11.95 eV, respectively. The computed spectra presented in this paper were simulated under aloof trajectories and only revealed the SPRs. Under aloof trajectories, the electron beam was passing outside of the target in the close vicinity to the outer edge where the bulk resonance was necessarily absent. However, the experimental EELS results were acquired under penetrating trajectories, therefore both surface and bulk plasmon resonances could be experimentally observed.

Supporting Information

Supporting Information is available from the Wiley Online Library or from the author.

Acknowledgements

P.M. and N.A. acknowledge Penn State MRSEC, Center for Nanoscale Science, under the award NSF DMR-1420620. A.G.N. and D.J.M. acknowledge support from the U.S. Department of Energy (DOE), Office of Science, Office of Basic Energy Sciences (BES), Materials Sciences and Engineering Division under award no. DE-SC0018040. T.S. acknowledges Swedish Research Council (grant no. 2015–06462). P.M.A. acknowledges support from the Air Force Office of Scientific Research under award number FA9550-18-1-0072. The authors thank Ke Wang at Penn State Materials Characterization Lab (MCL) for the electron microscopy support.

Conflict of Interest

The authors declare no conflict of interest.

Author Contributions

P.M. designed the study in consultation with N.A. P.M. carried out the STEM/EELS experiments and data analysis. A.G.N. and D.J.M. carried out the e-DDA simulations. T.S. and P.A. carried out the nanoplates synthesis work. T.B.v.D. carried out the SVD analysis. The manuscript was drafted by P.M. and edited by all co-authors.

Data Availability Statement

The data that support the findings of this study are available from the corresponding author upon reasonable request.

Keywords

Bi_2Te_3/Sb_2Te_3, defect-plasmon interaction, electron-driven discrete dipole approximation (e-DDA), low-dimensional tunable chalcogenides, monochromated electron energy loss spectroscopy (Mono-EELS), singular value decomposition (SVD), surface plasmon resonance

Received: September 14, 2021
Revised: January 27, 2022
Published online: March 24, 2022

---

[1] J.-Y. Ou, J. K. So, G. Adamo, A. Sulaev, L. Wang, N. I. Zheludev, *Nat. Commun.* **2014**, *5*, 5139.
[2] W. L. Barnes, A. Dereux, T. W. Ebbesen, *Nature* **2003**, *424*, 824.
[3] S. A. Maier, H. A. Atwater, *J. Appl. Phys.* **2005**, *98*, 011101.
[4] D. K. Gramotnev, S. I. Bozhevolnyi, *Nat. Photonics* **2010**, *4*, 83.
[5] M. Rothe, Y. Zaho, G. Kewes, Z. Kochovski, W. Sigle, P. A. van Aken, C. Koch, M. Ballauff, Y. Lu, O. Benson, *Sci. Rep.* **2019**, *9*, 3859.
[6] M. L. Brongersma, N. J. Halas, P. Nordlander, *Nat. Nanotechnol.* **2015**, *10*, 25.
[7] M. I. Stockman, K. Kneipp, S. I. Bozhevolnyi, S. Saha, A. Dutta, J. Ndukaife, N. Kinsey, H. Reddy, U. Guler, V. M. Shalaev, A. Boltasseva, B. Gholipour, H. N. S. Krishnamoorthy, K. F. MacDonald, *J. Opt.* **2018**, *20*, 043001.
[8] X. Lu, Q. Hao, M. Cen, G. Zhang, J. Sun, L. Mao, T. Cao, C. Zhaou, P. Jiang, X. Yang, X. Bao, *Nano Lett.* **2018**, *18*, 2879.
[9] J. Yin, H. N. S. Krishnamoorthy, G. Adamo, A. M. Dubrovkin, Y. Chong, N. I. Zheludev, C. Soci, *NPG Asia Mater.* **2017**, *9*, e425.
[10] A. M. Dubrovkin, G. Adamo, J. Yin, L. Wang, C. Soci, Q. J. Wang, N. I. Zheludev, *Adv. Opt. Mater.* **2017**, *5*, 1600768.
[11] A. Boltasseva, H. A. Atwater, *Science* **2011**, *331*, 290.
[12] G. V. Naik, V. M. Shalaev, A. Boltasseva, *Adv. Mater.* **2013**, *25*, 3264.
[13] J. Toudert, R. Serna, *Opt. Mater. Express* **2017**, *7*, 2299.
[14] T. Ginley, Y. Wang, Z. Wang, S. Law, *MRS Commun.* **2018**, *8*, 782.
[15] P. D. Pietro, M. Ortolani, O. Limaj, A. D. Gaspare, V. Giliberti, F. Giorgianni, M. Brahlek, N. Bansal, N. Koirala, S. Oh, P. Calvani, S. Lupi, *Nat. Nanotechnol.* **2013**, *8*, 556.
[16] H. Lu, S. Dai, Z. Yue, Y. Fan, H. Cheng, J. Di, D. Mao, E. Li, T. Mei, J. Zhao, *Nanoscale* **2019**, *11*, 4759.
[17] A. Vargas, F. Liu, S. Kar, *Appl. Phys. Lett.* **2015**, *106*, 243107.
[18] J. Guozhi, W. Peng, Z. Yanbang, C. Kai, *Sci. Rep.* **2016**, *6*, 25884.
[19] S. C. Liou, M.-W. Chu, R. Sankar, F.-T. Huang, G. J. Shu, F. C. Chou, C. H. Chen, *Phys. Rev. B* **2013**, *87*, 085126.
[20] J. J. Cha, K. J. Koski, K. C. Y. Huang, K. X. Wang, W. Duo, D. Kong, Z. Yu, S. Fan, M. L. Brongersma, Y. Cui, *Nano Lett.* **2013**, *13*, 5913.
[21] M. Zhao, M. Bosman, M. Danesh, M. Zeng, P. Song, Y. Darma, A. Rusydi, H. Lin, C.-W. Qiu, K. P. Loh, *Nano Lett.* **2015**, *15*, 8331.
[22] T. Ludwig, L. Guo, P. McCrary, Z. Zhang, H. Gordon, H. Quan, M. Stanton, R. M. Frazier, R. D. Rogers, H. T. Wang, C. H. Turner, *Langmuir* **2015**, *31*, 3644.
[23] T. Sharifi, S. Yazdi, G. Costin, A. Apte, G. Coulter, C. Tiwary, P. M. Ajayan, *Chem. Mater.* **2018**, *30*, 6108.
[24] H. J. Park, G. H. Ryu, Z. Lee, *Appl. Microsc.* **2015**, *45*, 107.
[25] A. Azizi, Y. Wang, G. Stone, A. L. Elias, Z. Liu, M. Terrones, V. H. Crespi, N. Alem, *Nano Lett.* **2017**, *17*, 2802.
[26] Y. Yonezu, K. Wakui, K. Furusawa, M. Takeoka, K. Semba, T. Aoki, *Sci. Rep.* **2017**, *7*, 12985.
[27] N. P. Blascetta, M. Liebel, X. Lu, T. Taniguchi, K. Watanabe, D. K. Efetov, N. F. van Hulst, *Nano Lett.* **2020**, *20*, 1992.
[28] A. Sajid, M. J. Ford, J. R. Reimers, *Rep. Prog. Phys.* **2020**, *83*, 044501.
[29] A. Genc, J. Patarroyo, J. Sancho-Parramon, N. G. Bastus, V. Puntes, J. Arbiol, *Nanophotonics* **2017**, *6*, 193.
[30] H. Oka, *Sci. Rep.* **2017**, *7*, 8047.
[31] M. Kociak, O. Stephan, L. Henrard, V. Charbois, A. Rothschild, R. Tenne, C. Colliex, *Phys. Rev. Lett.* **2001**, *87*, 075501.
[32] Q. Hao, C. Wang, H. Huang, W. Li, D. Du, D. Han, T. Qiu, P. K. Chu, *Sci. Rep.* **2015**, *5*, 15288.
[33] T. Coenen, A. Polman, *ACS Nano* **2014**, *8*, 7350.
[34] J. C. Prangsma, D. van Oosten, L. Kuipers, *Philos. Trans. R. Soc., A* **2011**, *369*, 3456.
[35] W. Sigle, J. Nelayah, C. T. Koch, B. Ogut, L. Gu, P. A. van Aken, *Ultamicroscopy* **2010**, *110*, 1094.
[36] D. Rossouw, G. A. Botton, *Opt. Express* **2012**, *20*, 6968.
[37] X. Sang, X. Li, W. Zhao, J. Dong, C. M. Rouleau, D. B. Geohegan, F. Ding, K. Xiao, R. R. Unocic, *Nat. Commun.* **2018**, *9*, 2051.
[38] Y. Fan, A. W. Robertson, Y. Zhou, Q. Chen, X. Zhang, N. D. Browning, H. Zheng, M. H. Rummeli, J. H. Warner, *ACS Nano* **2017**, *11*, 9435.
[39] C. Luo, X. Guo, H. Hu, D. Hu, C. Wu, X. Yang, Q. Dai, *Adv. Opt. Mater.* **2020**, *8*, 1901416.
[40] C. Schnell, *Nat. Methods* **2019**, *16*, 287.

[41] F. J. Gracia de Abajo, *Rev. Mod. Phys.* **2010**, *82*, 209.
[42] J. R. Jokisaari, J A. Hachtel, X. Hu, A. Mukherjee, C. Wang, A. Konecna, T. C. Lovejoy, N. Dellby, J. Aizpurua, O. L. Krivanek, J.-C. Idrobo, R. F. Klie, *Adv. Mater.* **2018**, *30*, 1802702.
[43] K. Imura, H. Okamoto, *Bull. Chem. Soc. Jpn.* **2008**, *81*, 659.
[44] L. Douillard, F Charra, Z. Korczak, R. Bachelot, S. Kostcheev, G. Lerondel, P.-M. Adam, P. Royer, *Nano Lett.* **2008**, *8*, 935.
[45] R. Gomez-Medina, N. Yamamoto, M. Nakano, F. J. Garcia de Abajo, *New J. Phys.* **2008**, *10*, 105009.
[46] P. Chaturvedi, K. H. Hsu, A. Kumar, K. H. Fung, J. C. Mabon, N. X. Fang, *ACS Nano* **2009**, *3*, 2965.
[47] A. Losquin, M. Kociak, *ACS Photonics* **2015**, *2*, 1619.
[48] J. Nelayah, M. Kociak, O. Stephan, F. J. G De Abajo, M. Tence, L. Henrard, D. Taverna, I. Pastoriza-Santos, L. M. Liz-Marzan, C. Colliex, *Nat. Phys.* **2007**, *3*, 348.
[49] D. Rossouw, M. Couillard, J. Vickery, E. Kumacheva, G. A. Botton, *Nano Lett.* **2011**, *11*, 1499.
[50] I M. Pavloveto, K. Aleshire, G. V. Hartland, M. Kuno, *Phys. Chem. Chem. Phys.* **2020**, *22*, 4313.
[51] Y. Zhang, L. P. Hu, T. J. Zhu, J. Xie, X. B. Zhao, *Cryst. Growth Des.* **2013**, *13*, 645.
[52] M. Zhao, J. Zhang, N. Gao, P. Song, M. Bosman, B. Peng, B. Sun, C.-W. Qiu, Q.-H. Xu, Q. Bao, K. P. Loh, *Adv. Mater.* **2016**, *28*, 3138.
[53] N. Peranio, E. Leister, W. Tollner, O. Eibl, K. Nielsch, *Adv. Funct. Mater.* **2012**, *22*, 151.
[54] V. B. Nascimento, V. E. de Carvalho, R. Paniago, E. A. Soares, L. O. Ladeira, H. D. Pfannes, *J. Electron Spectrosc. Relat. Phenom.* **1999**, *104*, 99.
[55] M. Scrocco, *J. Electron Spectrosc. Relat. Phenom.* **1990**, *50*, 171.
[56] J. Cunha, T.-L. Guo, G. D. Valle, A. N. Koya, R. P. Zaccaria, A. Alabastri, *Adv. Opt. Mater.* **2020**, *8*, 2001225.
[57] X. Kong, S. Albert, A. Bengoechea-Encabo, M. A. Sanchez-Garcia, E. Calleja, A. Trampert, *Nanotechnology* **2012**, *23*, 485701.
[58] T. B. van Driel, K. S. Kjaer, E. Biasin, K. Haldrup, H. T. Lemke, M. M. Nielsen, *Faraday Discuss.* **2015**, *177*, 443.
[59] G. A. Botton, J. A. Gupta, D. Landheer, J. P. McCaffrey, G. I. Sproule, M. J. Graham, *J. Appl. Phys.* **2002**, *91*, 2921.
[60] H.-K. Kim, H.-Y. Ha, J.-H. Bae, M. K. Cho, J. Kim, J. Han, J.-Y. Suh, G.-H. Kim, T.-H. Lee, J. H. Jang, D. Chun, *Sci. Rep.* **2019**, *10*, 13699.
[61] P. Potapov, A. Lubk, *Adv. Struct. Chem. Imaging* **2019**, *5*, 4.
[62] F. Fei, Z. Wei, Q. Wang, P. Lu, S. Wang, Y. Qin, D. Pan, B. Zhao, X. Wang, J. Sun, X. Wang, P. Wang, J. Wan, J. Zhou, M. Han, F. Song, B. Wang, G. Wang, *Nano Lett.* **2015**, *15*, 5905.
[63] F. de la Peña, et al., hyperspy/hyperspy: v1. 4. 2 (Version v1. 4. 2), https://org/10.5281/zenodo.3249885 (accessed: June 2019).
[64] A. Campos, N. Troc, E. Cottancin, M. Pellarin, H. C. Weissker, J. Lerme, M. Kociak, M. Hillenkamp, *Nat. Phys.* **2019**, *15*, 275.
[65] N. W. Bigelow, A. Vaschillo, V. Iberi, J. P. Camden, D. J. Masiello, *ACS Nano* **2012**, *6*, 7497.
[66] N. W. Bigelow, A. Vaschillo, J. P. Camden, D. J. Masiello, *ACS Nano* **2013**, *7*, 4511.